Available online at www.sciencedirect.com
ScienceDirect
Journal of Nuclear Materials 362 (2007) 364–373
journal of nuclear materials
www.elsevier.com/locate/jnucmat

Xenon migration behaviour in titanium nitride

S. Gavarini [a,*], N. Toulhoat [a,1], C. Peaucelle [a], P. Martin [b], J. Mende [a], Y. Pipon [a], H. Jaffrezic [a]

[a] IPN Lyon, UMR 5822, Domaine de la Doua, 4 rue Enrico Fermi, 69622 Villeurbanne cedex, France
[b] Centre d'Etudes de Cadarache, DEN/DEC/SESC/LLCC Bâtiment 151, 13108 Saint-Paul-lez-Durance, cedex, France

Abstract

Titanium nitride is one of the inert matrixes proposed to surround the fuel in gas cooled fast reactor (GFR) systems. These reactors operate at high temperature and necessitate refractory materials presenting a high chemical stability and good mechanical properties. A total retention of the most volatile fission products, such as Xe, I or Cs, by the inert matrix is needed during the in pile process. The thermal migration of xenon in TiN was studied by implanting 800 keV Xe^{++} ions in sintered samples at an ion fluence of 5×10^{15} cm^{-2}. Annealing was performed at temperatures ranging from 1673 to 1923 K for 1 and 3 h. Xenon concentration profiles were studied by Rutherford backscattering spectrometry (RBS) using 2.5 MeV α-particles. The migration behaviour of xenon corresponds to a gas migration model. It is dominated by a surface directed transport with a slight diffusion component. The mean activation energy corresponding to the diffusion component was found to be 2.2 ± 0.3 eV and corresponds to the Brownian motion of xenon bubbles. The directed Xe migration can be interpreted in term of bubble transport using Evans model. This last process is mostly responsible for xenon release from TiN.

PACS: 66.30.−h; 66.30.−Xj; 51.20.+d; 6182.Bg; 85.40.Ry

1. Introduction

Within the frame of the Generation IV project, two concepts of gas cooled reactors have been selected: the very high temperature reactor (VHTR) and the gas cooled fast reactor (GFR) [1–4]. In both cases, the fuel may operate at about 1273–1473 K in normal conditions and may reach 1873–1973 K in case of accident. Concerning the GFR concept, the fuel cycle has to be optimised to recycle actinides and to minimise the waste production. (Pu, U)C carbides and (Pu, U)N nitrides are candidates for the fuel kernel because of their high actinide density, and their elevated decomposition temperature and thermal conductivity [5,6]. Several geometries for the fuel assembly have been proposed for GFR, prismatic block or pebble bed for example, in which the fuel is surrounded by several coating layers and an inert matrix [7,8]. The principal criteria for the

* Corresponding author. Tel.: +33 472431464; fax: +33 4 72 44 80 04.
E-mail address: s.gavarini@ipnl.in2p3.fr (S. Gavarini).
[1] CEA/DEN.

0022-3115/$ - see front matter
doi:10.1016/j.jnucmat.2007.01.239

choice of the inert matrix are: chemical compatibility with the fuel, mechanical and irradiation resistance, thermal properties allowing high gas temperatures and total retention of fission products during the in pile process. The following ceramics, SiC, TiC, ZrC, TiN, ZrN [5–13], have been proposed for core structures in GFR reactor.

Titanium nitride is known as a material of choice for the coating of cutting and grinding tools as protection against wear, erosion and chemical attack [14–17]. It is also widely used in microelectronic instrumentation as diffusion barrier and adhesion promoter between metallic layers such as Al, Si, Cu, Ag or Pt [18–21]. The ability of titanium nitride to act as a diffusion barrier combined to its mechanical and thermal properties make it relevant for the previously described nuclear applications.

Few studies have been carried out on the retention properties of TiN for fission products and no diffusion coefficients have been reported in literature to our knowledge. Xenon is one of the most volatile fission products and is known to segregate in many materials because of its very low solubility [22–24]. In the case of UO_2, for example, Nicoll et al. [25] showed that the maximum solubility of xenon was about 10^{-5} at.%. Weber et al. [26] also observed a precipitation of gas bubbles at the TiN/Ti interface after irradiation with 250 keV Xe^+ ions at ion fluences of 10^{15}–10^{17} cm^{-2}. These last authors estimated the critical concentration for precipitation of xenon in titanium nitride to be less than 0.5 at.%. Different views still exist concerning the particular behaviour of precipitated gas bubbles in solids during annealing. For example, some authors consider gas bubble coarsening in UO_2 as a consequence of bubble migration and coalescence [27] whereas others invoke Ostwald ripening (thermal resolution) [28,29]. Concerning metals, Evans [30] explained the directed He-bubble diffusion observed by Marochov et al. [31] in nickel with a model based on thermal vacancy flow from free surfaces to bubble population. According to Evans, the directed motion of the gas bubbles toward the surface is also responsible for the dramatic acceleration of xenon release from UO_2 [30,32,33]. The aim of the present work is to study the thermally activated migration of xenon implanted into sintered titanium nitride. The evolution of the xenon concentration profile was characterized by RBS as a function of the temperature and the results are discussed in term of gas bubble behaviour.

2. Experimental

2.1. Sample preparation and annealing

Samples are sintered pellets of TiN $15 \times 15 \times 2\ mm^3$ in size. They are polished to micron using diamond powders. Sample density was found to be 5.18 (theoretical density = 5.39) $g\ cm^{-3}$ and major impurities are oxygen, about 2 at.%, and metals such as Fe and Ni, lower than 1 at.%.

In a first stage, pre- and post-implantation annealing of the samples was achieved, in a resistance tubular furnace, at 1273 K – 10 h and 1173 K – 10 h respectively, to relax the constraints and damages induced by polishing and ion implantation near the surface [34].

The second stage consists in annealing at higher temperatures, ranged from 1473 to 1923 K for 1 h (series 1: $T = 1673$ and 1773 K) and 3 h (series 2: $T = 1823$, 1873 and 1923 K), using a 12 kW EFD® induction heating system. In this system, the sample is supported by a tungsten susceptor disposed in a silica tube under a vacuum of about 10^{-7} mbar. The tube is then placed within the induction coil as represented in Fig. 1. The temperature is monitored using an Impac® bichromatic pyrometer. The infrared wavelengths used to determine the temperature are 0.9 and 1.1 μm. The emissivity ratio between both wavelengths was chosen to be 1.0 in the considered temperature range. The time needed to reach the annealing temperature was about 20 min in each case. During the heating ramp, the pressure never exceeded 5×10^{-6} mbar. At the end of the annealing, the power of the induction system was switched-off and the temperature of the sample decreased to the ambient in a few minutes.

2.2. Xenon implantation and RBS analysis

The xenon implantation was performed using the 400 kV accelerator of the Nuclear Physics Institute

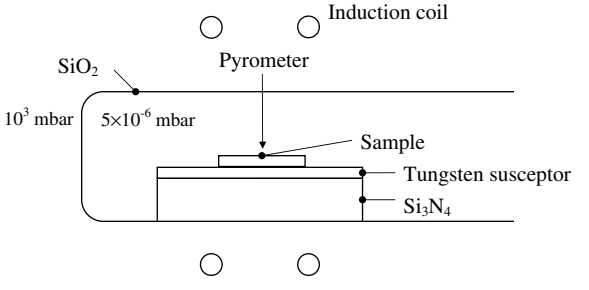

Fig. 1. Cross sectional scheme of the induction heating system.

of Lyon (IPNL) [35]. The implantation energy was 800 keV ($^{129}Xe^{++}$ ions) and the targeted implantation ion fluence was 5×10^{15} cm^{-2}. The ions were implanted under normal incidence and the implantation was performed at room temperature. An area of 25 cm^2 corresponding to the surface of about 10 samples was raster scanned at a beam current of 10 μA.

The as-implanted Xe depth profile distribution and the modified profiles after annealing were measured by RBS at the 4 MV Van de Graaff accelerator of the IPNL. The RBS spectra were collected using an $^4He^+$ incident ion beam with an energy of 2.5 MeV and a detection angle of 172°. The minimal intensity of the ion beam was used (i.e. $I \approx 10$ nA), in order to avoid any diffusion of xenon under α-irradiation.

3. Migration model and basic mechanisms

The model used to determine diffusion behaviour of xenon was based on the general transport equation [36,37]:

$$\frac{\partial C}{\partial t} = D\frac{\partial^2 C}{\partial x^2} + \langle v \rangle \frac{\partial}{\partial x}(C) + k \cdot C, \quad (1)$$

where C represents the elemental concentration, D the diffusion coefficient (cm^2 s^{-1}), $\langle v \rangle$ the average velocity (cm s^{-1}) of the elemental transport and k (s^{-1}) the loss coefficient. D, k and $\langle v \rangle$ are considered independent on the elemental concentration. To solve this equation the NAG Fortran library D03PCF/D03PCA subroutine was used [38].

The initial conditions given by $C(x,0)$ are represented by the as-implanted profile.

Eq. (1) is integrated within the space interval $[0,\infty]$ and within the time interval $[0, t_{max}]$.

Boundary conditions are given by $C(0,t)$ that is experimentally defined and constant, and by $\left(\frac{\partial C}{\partial x}\right)_{x=\infty} = 0$. D, k and $\langle v \rangle$ were adjusted to fit the model curves to the experimental profiles.

Eq. (1) is generally applied for single atom diffusion. The transport velocity ('$\langle v \rangle$' term) needs a driving force to occur, such as stress or thermal gradient for example. In the absence of any driving force, the only active components are the diffusion ('D' term) and eventually the loss component ('k' term). Concerning the particular case of gas bubbles, it is generally admitted that their motion requires the transfer of atoms around the bubble either by direct surface diffusion or by mass transfer trough the volume of the solid near the bubble [39–41]. In the absence of any driving forces, all these processes are random and thereby impose a Brownian motion on the bubble, depending on its radius and characterized by a global diffusion coefficient D_b. Conventional diffusion theory can then be applied to describe this Brownian motion considering a constant radius for the gas bubbles. The dependence on temperature of diffusion coefficients is then expressed in the form of an Arrhenius law:

$$D_b = D_0 \cdot \exp(-E_a/k_B T), \quad (2)$$

where D_0 is a pre-exponential term, k_B is the Boltzmann's constant, T the temperature and E_a the activation energy.

4. Results

4.1. Surface morphology

Fig. 2 shows the optical images and the scanning electron micrographs of the implanted surface after

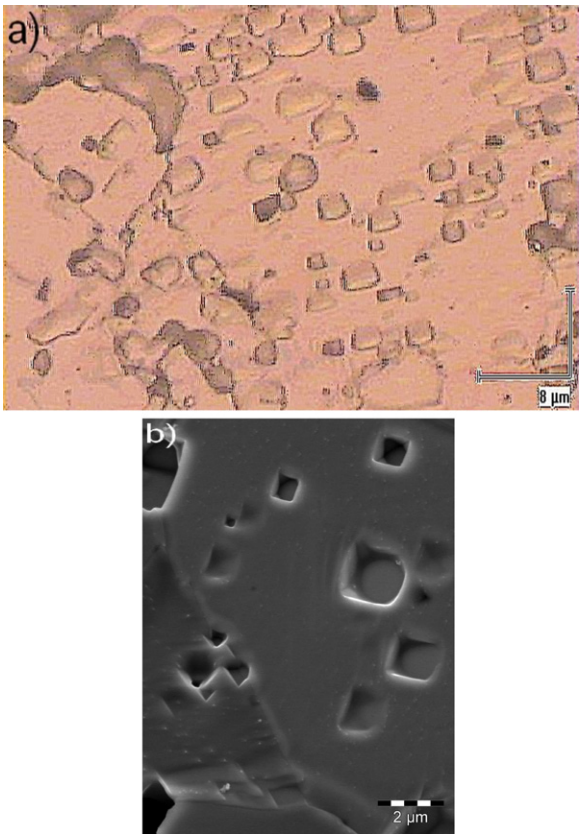

Fig. 2. Blisters and/or holes observed on sample surface after xenon implantation and annealing at 1923 K for 1 h: (a) optical microscope image, and (b) SEM micrograph.

annealing at the highest temperature, $T = 1923$ K, for 1 h. Micrometric blisters or holes were observed in the implanted area indicating the probable formation of gas bubbles during annealing. Note that blistering was also observed by Iseki and Kabeya [42] at the surface of TiC as a result of an increase of the internal pressure caused by the implantation of helium ions. From the near-square shapes on the surface it can be deduced that facetted bubbles were formed and migrated toward the surface during thermal treatment through the fcc structure of TiN.

4.2. RBS analysis

A typical RBS spectrum of the as-implanted TiN is represented in Fig. 3. The xenon peak is located at the high energy side due to its mass. The range and the straggle corresponding to the as-implanted xenon profile are slightly different from SRIM2003 code [43,44] simulation as shown in Table 1, probably because of unavoidable matter sputtering during implantation process. The implantation conditions lead to a maximum xenon concentration of about 0.3 at.%. A simulation of the experimental spectrum using SIMNRA software [45] indicated an implanted ion dose of $(4.3 \pm 0.3) \times 10^{15}$ cm^{-2}, which is slightly lower than the expected ion dose 5×10^{15} cm^{-2}, but remains comparable. In the following, the experimental dose has been taken into account, and all the comparisons after thermal treatments were done with respect to the 'as-implanted' experimental spectrum.

Table 1
Particle range and lateral straggle values for 800 keV $^{129}Xe^{++}$ implanted in TiN: (a) mean experimental value from RBS analysis, and (b) SRIM code calculation [34]

	Range (nm)	Straggle (nm)
Experiment	145 ± 4	66 ± 3
SRIM code	159 ± 1	45 ± 1

Fig. 4(a) and (b) presents the modifications of the xenon peak after each thermal treatment: Fig. 4(a) for series 1 and Fig. 4(b) for Series 2. For each series corresponding to a given duration of annealing, the xenon peak has moved to the high energies compared to the as-implanted signal and this displacement increases with temperature. Qualitatively, the shape of the xenon peak is also slightly modified after each annealing. The full width half maximum (FWHM) increases slightly with temperature in each series, which may indicate a slight diffusion of the implanted species. However the transport component remains clearly dominant, especially for high temperature annealing. The high energy side of the peak seems to be truncated after annealing at 1823 and 1873 K. It indicates a direct release of the transported xenon as it reaches the surface. After 1 h at 1923 K, a complete removal of the xenon from the sample is observed (dotted line in Fig. 4(b)).

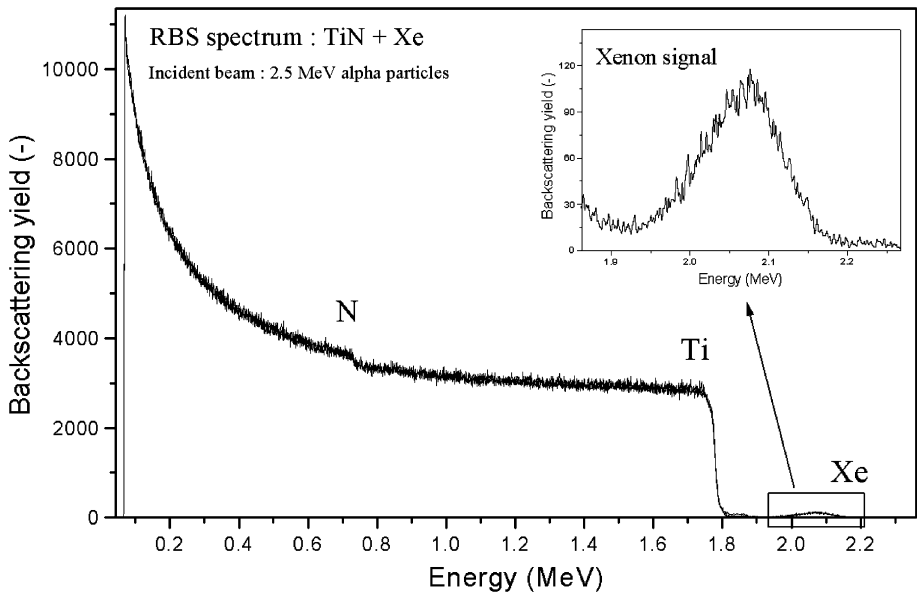

Fig. 3. RBS spectrum corresponding to the as-implanted TiN sample.

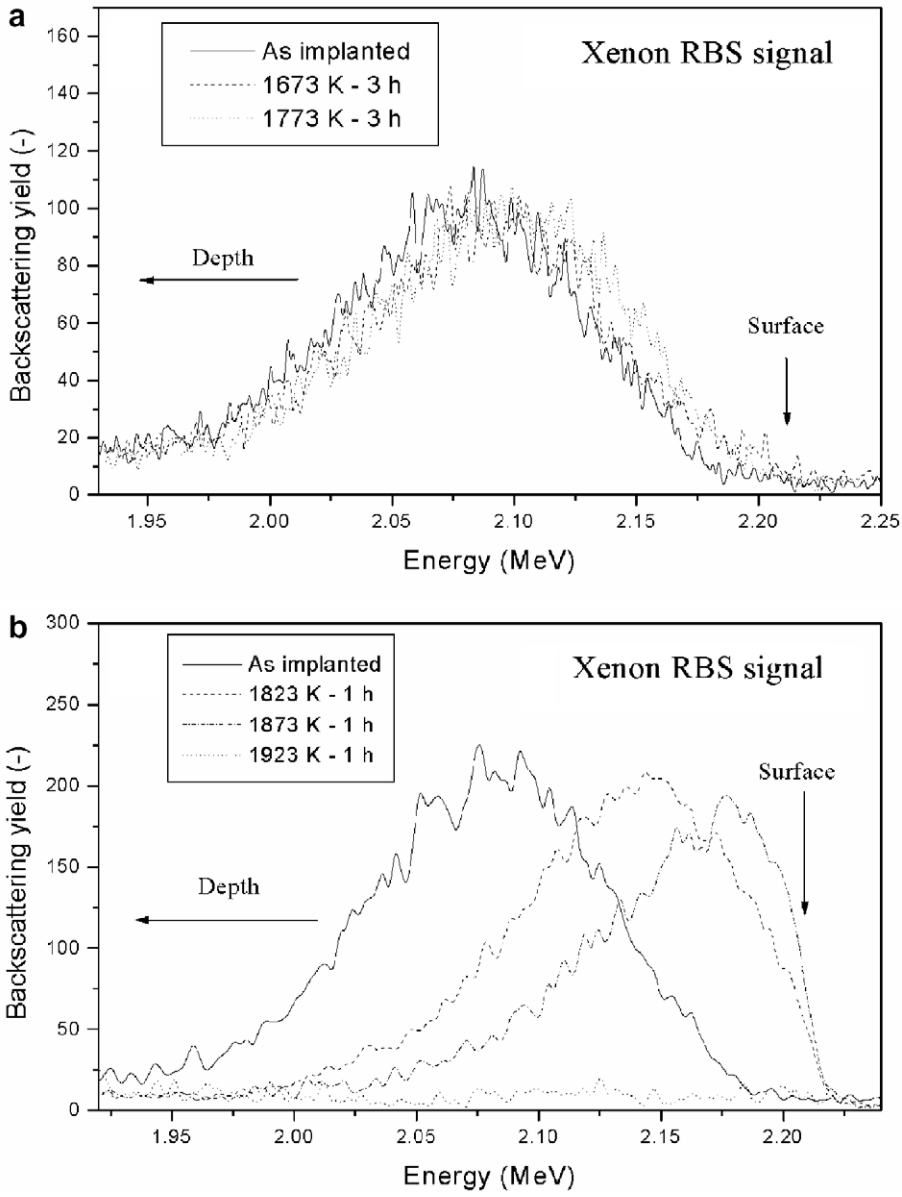

Fig. 4. Xenon RBS peak evolution during annealing at: (a) 1673 and 1773 K for 3 h (1st series), and (b) 1823, 1873 and 1923 K for 1 h (2nd series).

RBS spectra were processed using SIMNRA software to determine Xe depth distributions: Xe concentration (at.%) as a function of depth (nm), as presented in Fig. 5. These profiles were simulated using a FORTRAN routine (based on Eq. (1)) to obtain a quantitative information on the migration behaviour of xenon (dashed lines in Fig. 5). The resulting apparent diffusion coefficients D, average velocities of the elemental transport $\langle v \rangle$ and percentages of released xenon are summarized in Table 2. As it was observed qualitatively on RBS spectra displayed in Fig. 4, the transport velocity increases with the temperature (from $\langle v \rangle = 7.7 \pm 3.0 \times 10^{-11}$ cm s^{-1} at 1673 K to $\langle v \rangle > 7.7 \times 10^{-9}$ cm s^{-1} for $T > 1873$ K), and the loss of matter starts to become significant after 1 h at 1823 K (loss ranged from 25% to 100% between 1823 and 1923 K). The apparent diffusion coefficient values are displayed in Fig. 6 as a function of temperature. The points are highly dispersed around the linear fit

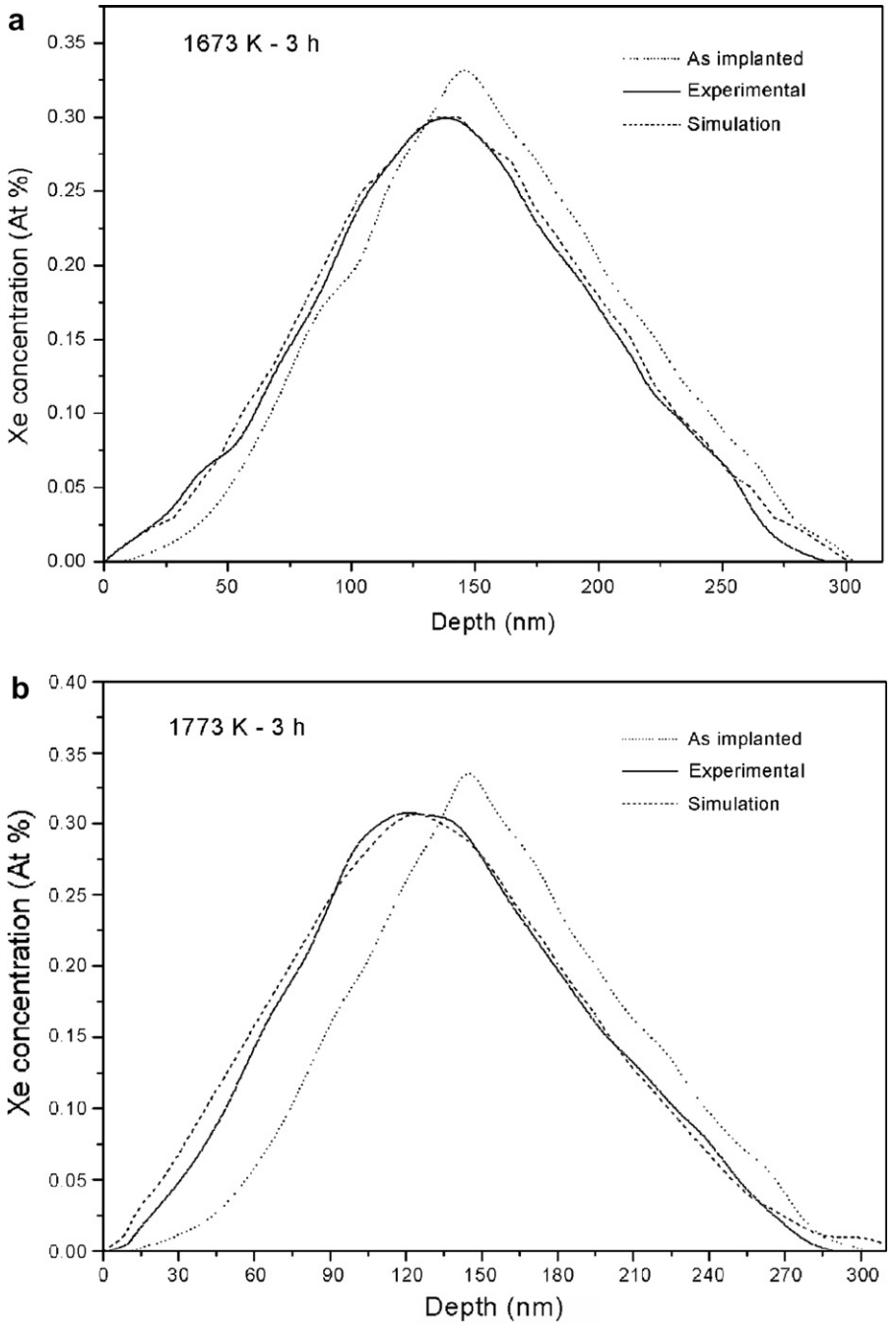

Fig. 5. Xenon experimental (solid line) and simulated (dashed line) depth distributions in TiN after thermal treatment at: (a) 1673 K, (b) 1773 K, (c) 1823 K and (d) 1873 K, together with the 'as-implanted' spectrum (dotted line).

(correlation coefficient: $r^2 = 0.703$) corresponding to the following equation $D = 7 \times 10^{-13} \cdot \exp(-2.2/k_B T)$, with k_B the Boltzmann's constant taken as $k_B = 8.65 \times 10^{-5}$ eV K^{-1}. According to this last equation the mean activation energy associated with the diffusion is $E_a = 2.2 \pm 0.3$ eV.

5. Discussion

SEM and optical microscope photographs displayed in Fig. 2 confirm that gas bubbles were formed as a consequence of the very low solubility of xenon. These bubbles have reached the surface

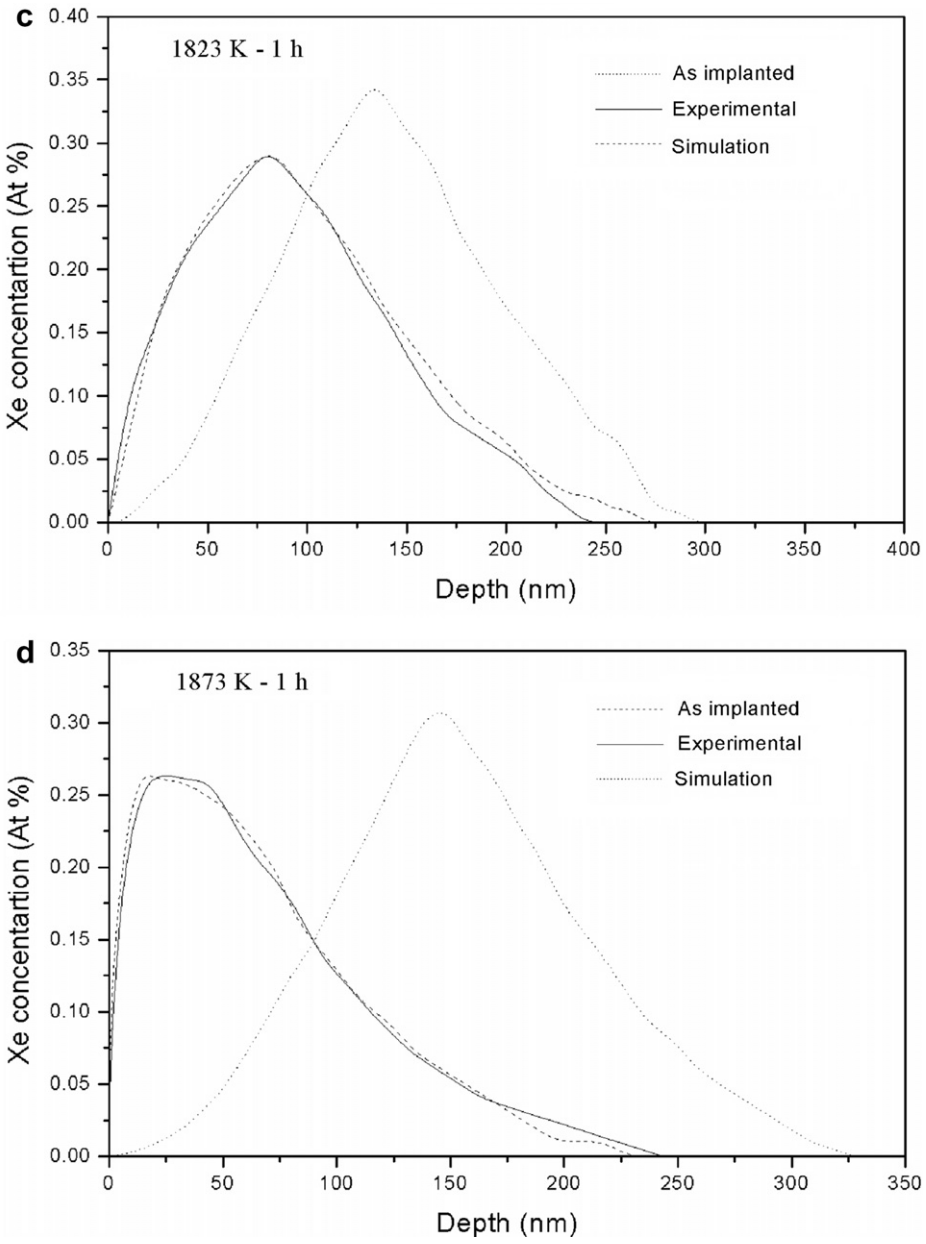

Fig. 5 (*continued*)

during thermal treatments at 1923 K, resulting in blistering or holes at the surface. The dimensions of the bubbles vary from a hundreds of nanometers to a few micrometers. Their dispersion in size is probably a consequence of the complex bubble coarsening taking place during annealing. The Evans model was applied to better understand the mechanisms involved in xenon bubbles migration [30,32,33]. According to this model, a vacancy concentration gradient exists between the main source of thermal vacancies (i.e. the surface in our case) and the nearby concentration of over-pressurized bubbles. This gradient induces an accelerated transport of the bubbles toward the surface relative to the normal random walk of the bubbles (Brownian motion). The Brownian motion of the bubbles could explain the observed diffusion component in our case. As indicated previously, diffusion of a bubble is usually described in term of surface diffusion or mass transfer through the volume [39–41]. Both

Table 2
Results of the migration modeling for xenon in TiN as a function of temperature: diffusion coefficient ($cm^2\ s^{-1}$), average velocity of the elemental transport ($cm\ s^{-1}$) and percentage of released xenon (%)

Temperature (K)	Duration (h)	Diffusion coefficient ($cm^2\ s^{-1}$)	Transport velocity ($cm\ s^{-1}$)	Fraction of released xenon (%)	Calculated transport velocity 'Evans model' ($cm\ s^{-1}$)
1673	3	$(1.7 \pm 0.2) \times 10^{-19}$	$(7.7 \pm 3) \times 10^{-11}$	<LOD[a]	1.8×10^{-10}
1773	3	$(1.8 \pm 0.2) \times 10^{-19}$	$(2.0 \pm 0.3) \times 10^{-10}$	<LOD	9.2×10^{-10}
1823	1	$(3.5 \pm 0.4) \times 10^{-19}$	$(1.9 \pm 0.3) \times 10^{-9}$	25 ± 5	1.9×10^{-9}
1873	1	$(1.05 \pm 0.2) \times 10^{-18}$	$(3.4 \pm 0.3) \times 10^{-9}$	85 ± 5	3.9×10^{-9}
1923	1	$>(1.05 \pm 0.2) \times 10^{-18}$	$>7.7 \times 10^{-9}$	≈100	7.8×10^{-9}

[a] LOD: limit of detection = 5%.

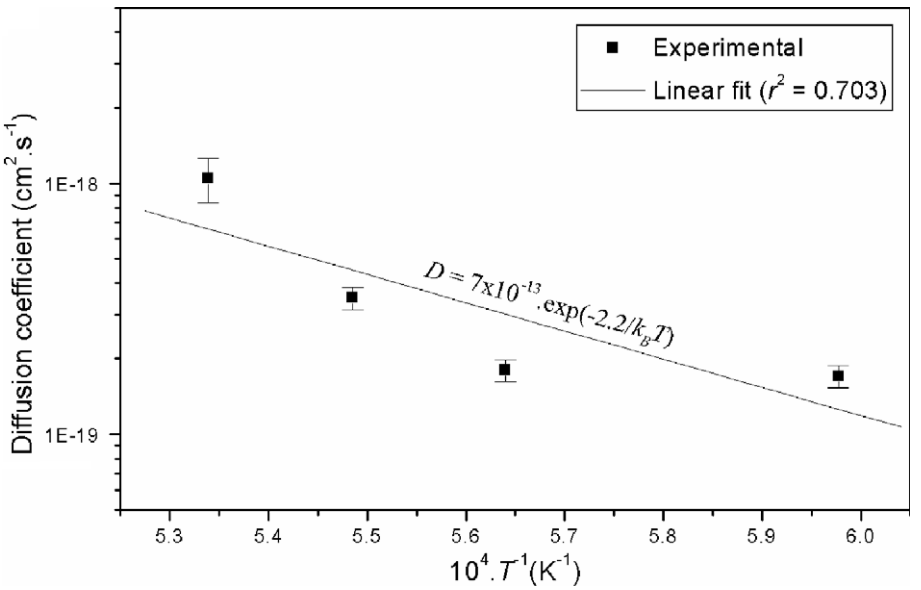

Fig. 6. Apparent diffusion coefficient values obtained from Eq. (1) (filled squares) together with a linear fit corresponding to the following equation $D = 7 \times 10^{-13} \cdot \exp(-2.2/k_B T)$, where D is the mean diffusion coefficient in $cm^2\ s^{-1}$, k_B the Boltzmann's constant taken as 8.65×10^{-5} eV K^{-1} and T the temperature in K.

mechanisms depend on bubble size which is varying in a complex way during annealing because of bubble coarsening. Moreover, the migration of the bubbles toward the surface induces changes in the boundary conditions (see Eq. (1)) and affects the homogeneity of the medium. Consequently, the calculated diffusion coefficients have to be considered as rough values. These facts could explain the non linear dependence on temperature of the apparent diffusion coefficients as represented in Fig. 6. As a matter of fact, the diffusion of xenon bubbles can hardly be described rigorously in our case from the simple laws displayed in Eqs. (1) and (2). However the use of these equations may provide interesting orders of magnitude for the diffusion coefficients and a mean value of the activation energy.

A directed motion of the xenon toward the surface was also clearly observed on experimental concentration profiles, superimposed with Brownian diffusion. This directed motion increases with temperature and could be linked to gas bubbles lying in the vacancy concentration gradient between the surface and the implanted zone as suggested by Evans [30,32,33]. As a consequence, bubbles acquire a velocity relative to the matrix. According to Evans, the formulation of Nichols [39] for the case of bubble motion in a temperature gradient can be used to treat the case of a vacancy gradient. Considering volume diffusion of the bubble to be the dominant process as in the case of UO_2 [30], this last formulation lead to the following expression for bubble velocity:

$$v_b = -2D_v \frac{C_s}{x}, \quad (3)$$

where D_v is the volume self-diffusion coefficient of the vacancies, C_s the vacancy concentration at the surface, and x the depth of the considered bubble layer. Note that this expression is independent of the bubble size in contrast to the previous case. However, Van Siclen [46] indicated that some deviations from Eq. (3) may occur for bubble configurations with distances to the surface, or to each other, smaller than the bubble diameter. To simplify the model this last assumption was not considered and bubble velocity v_b was calculated in a first approximation on the basis of Eq. (3). Known values of nitrogen diffusion coefficients in δ-phase of titanium nitride (D_v) and associated migration energy of vacancies (E_v) were used as displayed in the following references [34,47,48]: $D_v = 5.4 \times 10^{-3} \cdot \exp(-E_v/k_B T)\,\mathrm{cm^2\,s^{-1}}$ and $E_v = 2.1$ eV (mean value from literature data). The experimental range of the implanted xenon ions (see Table 1) was taken as the mean depth of the implanted layer: $x =$ 145 nm, and the nitrogen vacancy concentration at the surface for a given temperature T was taken as: $C_s^T = \exp(-E_v/k_B T)$. The resulting calculated velocities, displayed in Table 2, are close to the experimental values for each temperature. As a consequence, it may appear reasonable to interpret xenon migration mechanism as an upward flow of gas bubbles toward the surface together with a downward flow of thermal vacancies. This mechanism is clearly and mainly responsible for the removal of xenon from the sample at high temperature. Even if the accelerated release of fission gases at high concentration has to be taken into account for many materials, it is worth to note that in the case of low concentrations, single atom diffusion is expected and may result in a lower elemental release. To confirm this last point, complementary implantations with radioactive ^{133}Xe will be carried out at a low ion fluence of about $10^{10}\,\mathrm{cm^{-2}}$.

6. Conclusion

Thermal migration of xenon implanted in sintered titanium nitride was studied up to 1923 K. An oriented transport toward the surface was observed superimposed with the Brownian motion of xenon bubbles. The activation energy associated with the Brownian motion was found to be 2.2 ± 0.3 eV whereas the directed transport velocity $\langle v \rangle$ was found to range from $(7.7 \pm 3.0) \times 10^{-11}$ to $7.7 \times 10^{-9}\,\mathrm{cm\,s^{-1}}$ for temperatures in the range 1673–1873 K. The migration behaviour of xenon can be satisfactorily interpreted in term of bubble transport using Evans model. According to this model, the vacancy concentration gradient existing between the main source of thermal vacancies (i.e. the surface in our case) and the nearby concentration of over-pressurized bubbles is responsible for the accelerated transport of the bubbles towards the surface and it results in a complete removal of xenon from the matrix after 1 h at 1923 K.

Acknowledgements

The authors thank A. Perrat-Mabilon, A. Gardon, Y. Champelovier and R. Fillol from the 'accelerator group' of the IPNL for their contribution. Thanks are also due to N. Moncoffre for having read this article before submission and having given some useful corrections. The author personally thanks J.H. Evans for the help provided through his articles.

References

[1] P. Hejzlar, M.J. Pope, W.C. Williams, M.J. Driscoll, Prog. Nucl. Energy 47 (2005) 271.
[2] P. Billot, D. Barbier, in: Proceedings of the Second International Topical Meeting on High Temperature Reactor Technology, Beijing, China, September 22–24 2004.
[3] A Technology Roadmap for Generation IV Nuclear Energy Systems, Issued by the US DOE Nuclear Energy Research Advisory Committee and the Generation IV International Forum, December 2002.
[4] Generation IV International Forum Website: <http://gif.inel.gov/roadmap/>.
[5] M. Streit, F. Ingold, J. Eur. Ceram. Soc. 25 (2005) 2687.
[6] K. Minato, M. Akabori, M. Takano, Y. Arai, K. Nakajima, A. Itoh, T. Ogawa, J. Nucl. Mater 320 (2003) 18.
[7] J. Porta, P. Lo Pinto, M. Bonnet, K. Kugeler, Z. Alkan, R. Heuss, W. von Lensa, Prog. Nucl. Energy 38 (2001) 407.
[8] C. Guéneau, S. Chatain, S. Gossé, C. Rado, O. Rapaud, J. Lechelle, J.C. Dumas, C. Chatillon, J. Nucl. Mater. 344 (2005) 191.
[9] Y. Arai, K. Nakajima, J. Nucl. Mater. 281 (2000) 244.
[10] N. Chauvin, R.J.M. Konings, Hj. Matzke, J. Nucl. Mater. 274 (1999) 105.
[11] H. Nabielek, W. Schenk, W. Heit, A.-W. Mehner, D.T. Goodin, Nucl. Technol. 84 (1989) 62.
[12] K. Minato, T. Ogawa, K. Fukuda, H. Nabielek, H. Sekino, Y. Nozawa, I. Takahashi, J. Nucl. Mater. 224 (1995) 85.
[13] L.C. Walters, D.L. Porter, D.C. Crawford, Progr. Nucl. Energy. 40 (2002) 513.
[14] H.O. Pierson, Handbook of Refractory Carbides and Nitrides, Noyes Publications, 1996.
[15] H.C. Brashilia, A. Jain, K.S. Rajam, Vacuum 72 (2004) 241.

[16] S.A. Barnett, A. Madan, Scr. Mater. 50 (2004) 739.
[17] S. Chatterjee, T.S. Sudarshan, S. Chandrashekhar, J. Mater. Sci. 27 (1992) 1989.
[18] P. Patsalas, S. Logothetidis, J. Appl. Phys. 90 (2001) 4725.
[19] L. Gao, J. Gstöttner, R. Emling, M. Balden, Ch. Linsmeier, A. Wiltner, W. Hansch, D. Schmitt-Landsiedel, Microelectron. Eng. 76 (2004) 76.
[20] Y.-H. Shin, Y. Shimogaki, Sci. Technol. Adv. Mater 5 (2004) 399.
[21] S.-K. Rha, W.-J. Lee, S.-Y. Lee, Y.-S. Hwang, Y.-J. Lee, D.-I. Kim, D.-W. Kim, S.-S. Chun, C.-O. Park, Thin Solids Films 320 (1998) 134.
[22] C. Degueldre, M. Pouchon, M. Döbeli, K. Sickafus, K. Hojou, G. Ledergerber, S. Abolhassani-Dadras, J. Nucl. Mater. 289 (2001) 115.
[23] L.M. Wang, S. Zhu, S.X. Wang, R.C. Ewing, N. Boucharat, A. Fernandez, Hj. Matzke, Prog. Nucl. Energy 38 (2001) 295.
[24] C. Degueldre, Ch. Hellwig, J. Nucl. Mater. 320 (2003) 96.
[25] S. Nicoll, H.J. Matzke, C.R.A. Catlow, J. Nucl. Mater. 226 (1995) 51.
[26] Th. Weber, W. Bolse, K.P. Lieb, Nucl. Instrum. and Meth. B 50 (1990) 95.
[27] V.F. Chkuaseli, Hj. Matzke, J. Nucl. Mater. 201 (1993) 92.
[28] S. Kashibe, K. Une, K. Nogita, J. Nucl. Mater. 206 (1993) 22.
[29] H. Schroeder, P.F.P. Fichtner, J. Nucl. Mater 179–181 (1991) 1007.
[30] J.H. Evans, J. Nucl. Mater. 210 (1994) 21.
[31] N. Marochov, L.J. Perryman, P.J. Goodhew, J. Nucl. Mater. 149 (1987) 296.
[32] J.H. Evans, J. Nucl. Mater. 225 (1995) 302.
[33] J.H. Evans, A. van Veen, J. Nucl. Mater. 233–237 (1996) 1179.
[34] F. Elstner, H. Kupfer, F. Richter, Phys. Status Solidi 147 (1995) 373.
[35] Website of the Nuclear Physics Institute in Lyon (IPNL) – France: <http://lyoinfo.in2p3.fr/ace>.
[36] J. Philibert, Diffusion et transport de matière dans les solides, les éditions de Physique (1985).
[37] J. Crank, The Mathematics of Diffusion, 2nd Ed., Oxford Sience Pblications, 1975.
[38] M. Berzins, Developments in the NAG Library Software Systems, in: J.C. Mason, M.G. Cox (Eds.), Chapman and Hall, 1990, p. 59.
[39] F.A. Nichols, J. Nucl. Mater. 30 (1969) 143.
[40] F.A. Nichols, Acta Meter. 20 (1972) 207.
[41] Ya. E. Geguzin, M.A. Krivoglas, Migration of Macroscopic Inclusions in Solids, Consultants Bureau, New-York and London, 1973.
[42] M. Iseki, Z. Kabeya, J. Nucl. Mater. 133&134 (1985) 722.
[43] J.P. Biersack, L.G. Haggmark, Nucl. Instrum. and Meth. B (1980) 174.
[44] <http://www.srim.org>.
[45] M. Mayer, SIMNRA™ User's guide, Technical report IPP 9/113, 1997, Max Planck Institut für Plasmaphysik Garching.
[46] C.DeW. Van Siclen, Philos. Mag. Lett. 72 (1995) 41.
[47] A. Gicquel, N. Laidani, P. Saillard, J. Amouroux, Pure Appl. Chem. 62 (1990) 1743.
[48] F.W. Wood, O.G. Paasche, Thin Solids Films 40 (1977) 131.